Acid-Base Interactions, Vol. 2, pp. 223–234
Ed. K.L. Mittal

Acid–base interactions at the molecular level: Adhesion and friction studies with interfacial force microscopy

A. R. BURNS,* J. E. HOUSTON, R. W. CARPICK and T. A. MICHALSKE

Surface and Interface Sciences Department, Sandia National Laboratories, Albuquerque, NM 87185-1413, USA

Abstract—To examine the forces of acid–base adhesion interactions at a molecular level, we have utilized the scanning probe Interfacial Force Microscope (IFM). Unlike cantilever-based atomic force microscopes, the IFM is a non-compliant, mechanically stable probe that provides a complete adhesion profile without jump-to-contact. In this way, we are able to quantitatively measure the work of adhesion and bond energies at well-defined, nanometer-scale single asperity contacts. In particular, we will discuss the displacement-controlled adhesion forces between self-assembled monolayers of functionalized alkanethiols strongly bound to a gold substrate and a similarly functionalized tip. We also discuss a method utilizing decoupled lateral and normal force sensors to simultaneously observe the onset of both friction and chemical bond formation. Measurements show that friction can be directly attributed to bond formation and rupture well before repulsive contact.

Keywords: Adhesion; friction; scanning probe microscopy; interfacial forces; interfacial force microscopy.

1. INTRODUCTION

In the last ten years, the field of scanning probe force microscopy of surfaces has grown enormously. The primary factors in this growth stem from the realization that attractive and repulsive forces between the probe tip and the sample surface can be utilized to provide not only a "feedback" signal for detailed nanometer-scale topographic imaging, but also to provide a window into those molecular force interactions with nN sensitivity and unprecedented displacement and lateral resolutions. Atomic force microscopes (AFM) [1–3] and interfacial force microscopes (IFM) [4, 5], can detect weak van der Waals forces as well as strong bonding interactions. Fundamental studies of friction and tribology have undergone a considerable rebirth due to the ability of scanning probe microscopes to detect lateral forces simultaneously with normal forces [6–8], although the fundamental relationship between friction and adhesion remains elusive.

* To whom correspondence should be addressed: E-mail: aburns@sandia.gov

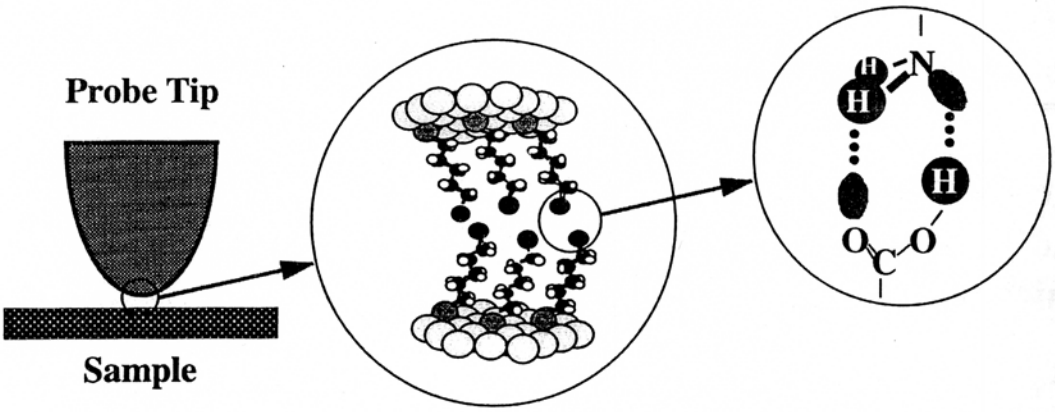

Figure 1. Schematic representation of scanning probe studies of (acid–base) hydrogen bonding between functional groups terminating alkanethiol monolayers. The thiol monolayers self-assemble on gold substrates, thus both tip and sample are initially coated with gold.

Chemical modification of the sample and/or scanning probe tip with hydrophobic or hydrophilic functional groups has been shown to be a sensitive way to probe "chemical forces" and to map the location of functional groups [5, 9–11]. An extremely effective and reproducible way of tailoring functional groups for fundamental studies of adhesion is to use self-assembled monolayers of n-alkanethiols [12, 13] that are terminated with various tail groups such as CH_3, COOH, OH, NH_2. A schematic representation is shown in Fig. 1. Alkanethiols have also been used extensively as model "lubricants" because they can be tailored to examine dissipative losses as a function of "mechanical" parameters such as chain length, packing density [7, 14], and cross-linking [15], as well as "chemical" parameters such as molecular adhesion.

In this paper we will discuss how the IFM can be used to study adhesion interactions at the molecular level. Extensive reviews of cantilever-based AFM studies can be found in Refs. [7, 10]. The IFM was developed [4] to overcome the inherent mechanical instabilities of AFM cantilevers when making ("jump-to-contact") and breaking ("pull-off") interfacial contacts. As shown in Fig. 2, these instabilities arise when the attractive force gradient of the tip-sample interaction exceeds the spring constant of the cantilever. Much of the detail in the adhesion force-distance profile is lost when these mechanical instabilities occur, and the contact itself always has some repulsive character [16]. Another concern is the phenomenon of adhesion hysteresis, which is the reason that we show *two* force *vs.* displacement curves in Fig. 2 instead of a single curve. The causes of hysteresis go beyond the scope of this paper, but can be attributed to irreversible mechanical, chemical, and/or structural effects [17]. On approach, the jump-to-contact can completely obscure the depth of the initial, bond-forming adhesion interaction; whereas on withdrawal, the much stronger adhesion interaction is observed directly as the pull-off force. In fact, it is the pull-off force that is commonly used to determine the work of adhesion (see Equation (1) in next section). Thus we see that in the case of significant adhesion hysteresis, AFM analysis of adhesion energies must be viewed with caution. Furthermore, mechanical impact resulting from jump-to-contact may significantly alter the character of the adhesion interface. It is clearly desirable to have a mechanically stable, displacement-controlled

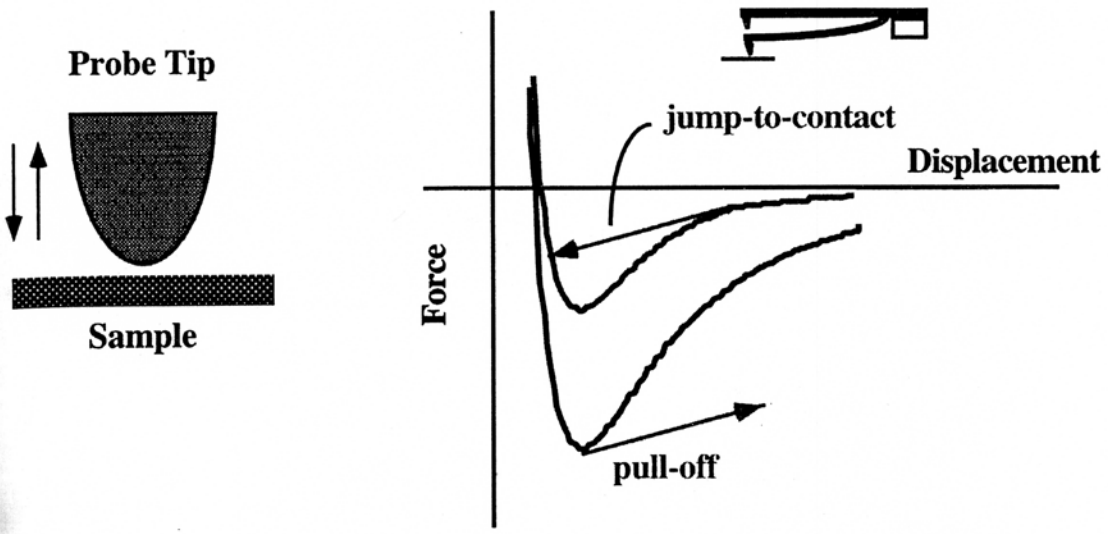

Figure 2. Schematic representation of force profile during tip approach to sample and during withdrawal after repulsive contact. Cantilevered AFM tips shown at top will suffer from "jump-to-contact" if the approach force gradient exceeds the cantilever spring constant (slope of arrow). Similarly, the cantilever will exhibit the "pull-off" instability during withdrawal from contact. Note that the approach and withdrawal curves are not the same if there is significant adhesion hysteresis.

method to measure the tip-sample adhesion interaction. While we exclusively discuss adhesion force vs. displacement experiments here, we still retain the advantages of nanoscale resolution and imaging capabilities of scanning probe microscopy.

2. INTERFACIAL FORCE MICROSCOPY

The basic idea underlying an IFM is shown in Fig. 3. Details concerning operation of the sensor may be found elsewhere [4, 18], and are only briefly summarized here. An IFM sensor consists of a teeter-totter-like common plate of a differential capacitor suspended by torsion bars above two identical gold pads fixed in a glass substrate, creating capacitances C_1 and C_2 in Fig. 3. The position of the common plate is determined by an rf bridge circuit and is initially balanced by static voltages applied to the capacitor pads. The balanced sensor is placed under proportional-integral-derivative feedback control by a circuit that supplies voltages to one pad to counteract any error signal due to normal forces applied by the tip. The normal force can be directly calculated with reasonable accuracy and precision (±20%) from the feedback voltage, the capacitances, and the static voltages, or it can be directly calibrated (with greater accuracy and precision) using a laboratory microbalance [4, 18]. Unlike AFM cantilevers, the sensor is mechanically stable and non-compliant. Scanning and displacement-controlled approaches and withdrawals are performed with standard piezoelectric devices.

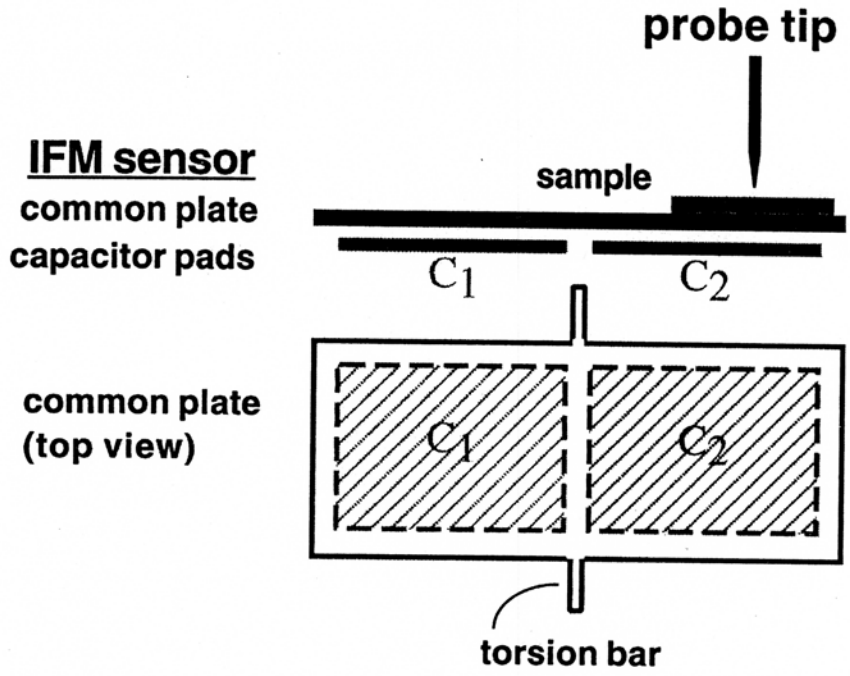

Figure 3. Schematic of interfacial force microscope (IFM). A probe tip is brought into contact with a sample resting on an IFM sensor. The sensor measures the attractive and repulsive normal forces on the tip by maintaining an electrostatic balance of two capacitors C_1 and C_2, formed by the common plate and identical gold pads fixed on a glass substrate (not shown).

Representative force-displacement curves [5] in the tip/sample adhesion interaction are shown in Fig. 4. These experiments were performed in an atmosphere of dry nitrogen. For these data, various pairs of thiol tail groups were prepared on the gold-coated probe tips and samples by 24-hour exposure to 0.5 mM solutions of specific n-alkanethiols $X(CH_2)_{11}SH$, where $X=CH_3$, NH_2, COOH. The force profiles were measured at a displacement rate of 8 nm/s, and the zero of displacement was arbitrarily set as the point where the IFM signal (load) goes through zero prior to positive (net repulsive) loading. It was also convenient for further evaluation to normalize the adhesion forces relative to the tip radius (Equation (1)) in order to scale results for the different tip radii measured beforehand by scanning electron microscopy and shown in parentheses. Qualitatively, one can see that a complete range of adhesion interaction between tip and sample was obtained for both approach and withdrawal, with no evidence of mechanical instabilities. The adhesion forces increase considerably in the expected order as one progresses from the CH_3 *vs.* CH_3 van der Waals interaction to the full two-center acid–base bonding in NH_2 *vs.* COOH.

Quantitative analysis of the force-displacement curves is based on the following. From contact mechanics, the work of adhesion W_A between the parabolic tip with radius R and the sample is a function of the critical load L_c (usually negative), or peak attractive force, at pull-off:

$$W_A = \frac{-L_c}{\pi CR}. \tag{1}$$

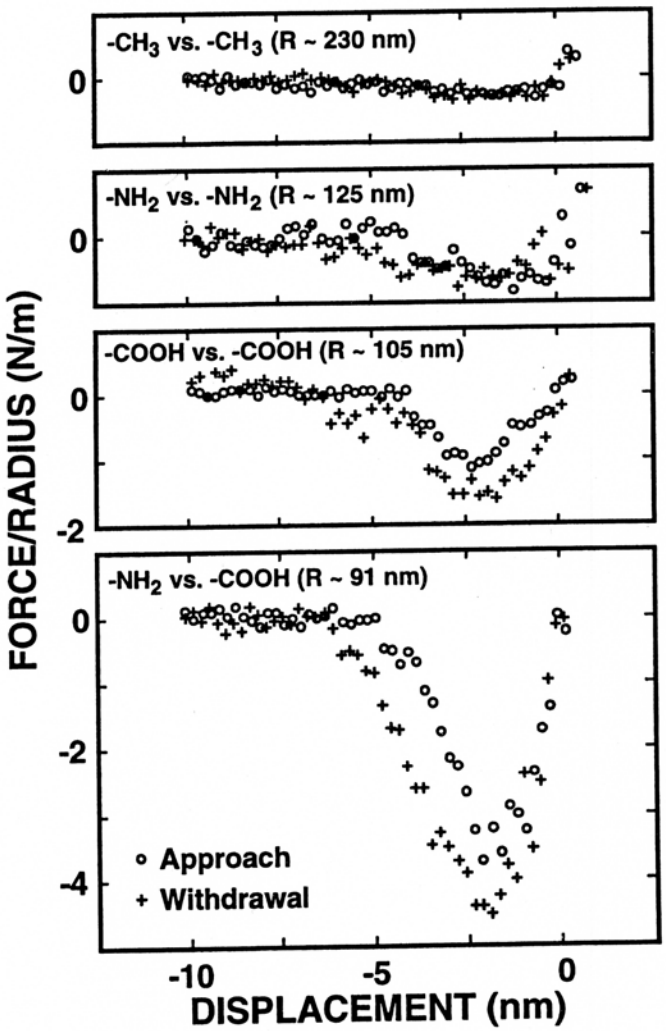

Figure 4. Force-displacement approach (O) and withdrawal (+) curves for various pairings of functional terminal groups of alkanethiols (from Ref. [5]). From top to bottom these are CH_3 *vs.* CH_3, NH_2 *vs.* NH_2, COOH *vs.* COOH, and COOH *vs.* NH_2. The force axis is normalized to the probe radius R, thus proportional to the work of adhesion (Equation (1)). Zero displacement is arbitrarily chosen to be the point where the force goes through zero at contact (far right). Approach is from left to right.

The constant $C = 3/2$ in the Johnson, Kendall, Roberts (JKR) [19] model of adhesion contact mechanics, whereas $C = 2$ in the Derjaguin, Muller, Toporov (DMT) [20] model. Much controversy has surrounded the applicability of one model over the other and scanning probe experiments often require elements of both. We use the JKR model here because it correctly predicts a finite contact area at the critical load L_c, while the DMT model predicts zero contact area at L_c. This becomes important in the next section where we discuss friction *vs.* load. In Fig. 4, (L_c/R) is usually larger for the withdrawal relative to the approach because of adhesion hysteresis. It is well known from the Dupré equation (Equation 2) [17] that the work of adhesion W_A is a

function of the surface free energies γ_1 and γ_2 of the contacting surfaces and the interfacial free energy γ_{12}:

$$W_A = \gamma_1 + \gamma_2 - \gamma_{12}. \tag{2}$$

For identical pairs of interfaces, $\gamma_1 = \gamma_2$ and $\gamma_{12} = 0$; hence, W_A becomes the work of cohesion $2\gamma_1$ and we obtain the surface free energies γ_1 shown in Table 1. The CH_3 *vs.* CH_3 pair is expected to have a purely van der Waals (dispersive) interaction, with each monolayer having a surface free energy of ~ 25 mJ/m^2 [17]. We see that the result is too high (it would be much closer to the expected value if $C = 2$). The other two identical pairs indicate increasing surface free energies due to hydrogen-bonding contributions. Fowkes [21] realized that contributions to the surface free energy could be additive, i.e.

$$\gamma_1 = \gamma_1^d + \gamma_1^h, \tag{3}$$

where the first term in Equation (3) is the non-directional dispersion forces contribution, and the second term is the directional hydrogen-bonding contribution.

Table 1.
Summary of IFM adhesion experiments

Interface	W_A (mJ/m^2)	γ_1 or γ_{12} (mJ/m^2)	H-bonding (mJ/m^2)	Bond energy (kcal/mole)	Gas phase* (kcal/mole)
CH_3 vs. CH_3	80±43	40±21 (γ_1)			
NH_2 vs. NH_2	133±32	67±16 (γ_1)	53±32	1.6±1.0	3.4
COOH vs. COOH	304±72	152±36 (γ_1)	224±72	6.9±2.2	14.0
COOH vs. CH_3	80±43	0 (γ_{12})			
COOH vs. NH_2	907±83	-688±41 (γ_{12})	688±41	21.1±1.3	

* From Ref. [22].

To estimate the latter for the pairs NH_2 *vs.* NH_2 and COOH *vs.* COOH we simply subtract the 80 mJ/m^2 dispersion contribution measured from the hydrophobic CH_3 *vs.* CH_3 pair (see Table 1) which has no bonding; i.e., $\gamma_1 = \gamma_1^d$ = 40 mJ/m^2. We show below that the dispersive component is the same for the COOH and CH_3 tail groups. The homologous pairs indicate very weak hydrogen bonding in the NH_2 vs. NH_2 case and relatively stronger bonding in COOH *vs.* COOH case. In order to compare the results in Table 1 with gas-phase values, we convert the bond energy per unit area (mJ/m^2) to kcal/mole by assuming a uniform molecular spacing of 21.4 Å^2/molecule. The gas-phase energetics for dimerization of NH_2 *vs.* NH_2 and COOH *vs.* COOH are, respectively, 3.4 kcal/mole and 14 kcal/mole [22], which are roughly twice that estimated here. However, the gas-phase value for the latter represents two bonds per dimer. It is possible that the discrepancy may be due to hydrogen-bonding between NH_2 (or COOH) groups within the same monolayer and/or steric constraints for close-packed monolayers that do not permit optimum bonding orientation.

The work of adhesion of hydrocarbon/polar interfaces such as CH_3 *vs.* COOH can be estimated from the purely dispersive contributions [17, 21] through

$$W_A \approx 2\sqrt{\gamma_1^d \gamma_2^d} \ . \qquad (4)$$

Since W_A is the same for the CH_3 *vs.* COOH pair and the CH_3 *vs.* CH_3 pair, the van der Waals components for the two tail groups are indistinguishable and thus no other interaction was significant. Since $W_A = 2\gamma_1^d$ for the CH_3 *vs.* CH_3 pair, we obtain from Equation (4) that $W_A = 2\gamma_1^d$. It is important to note that analogous experiments [9, 10] performed in a liquid such as water or ethanol will have three interfaces and thus very different results.

We finally obtain evidence for a true acid/base interaction with the pair COOH *vs.* NH_2. The large work of adhesion for this pair in Fig. 4 is due to the interfacial free energy γ_{12}. From Equation (2) and the values of γ_1 and γ_2 obtained from Table 1, we estimate γ_{12} = -688 mJ/m^2. We saw from the CH_3 *vs.* COOH pair that van der Waals interactions could be neglected in γ_{12}, thus we attribute the entire amount to hydrogen bonding. This value corresponds to ~21 kcal/mole, which is certainly in the range of strong hydrogen bonding [17], and is consistent with the increased polarity of the two-center interaction (see Fig. 1) relative to the COOH *vs.* COOH dimer.

Thus we have shown that the IFM technique is sensitive to the strength of interfacial bonding as well as being capable of monitoring the entire adhesion interaction. As pointed out elsewhere [10], a distinct advantage of scanning probe adhesion studies is the ability to probe the surface energies of high free energy surfaces. These materials are not amenable to contact angle analysis because they are wet by most liquids. Furthermore, contact angle measurements are macroscopic and thus do not necessarily account for surface roughness [17]. However, an important issue in both AFM and IFM studies is the presence of trace water monolayers condensed from the atmosphere, even when the conditions are "inert". Water layers can potentially reduce surface energies, particularly for strongly hydrophilic surfaces. The results discussed here thus represent a lower bound to the binding energies.

3. FRICTION MEASUREMENTS WITH INTERFACIAL FORCE MICROSCOPY

Scanning probes can also be used in sliding contacts to measure friction on the nanometer scale. The effects of adhesion on the *lateral* forces experienced by scanning probes has been an active area not only because of model lubricant studies, but also because this is the basis for "chemical force" imaging of functional groups [7, 9, 10]. Unfortunately, the mechanical instabilities of cantilever-based measurements tend to obscure the exact relation between friction, interfacial bonding, and applied load. That is because the friction forces are generally measured only in the repulsive regime of the contact, or for a limited range preceding pull-off that has both repulsive and attractive components [16]. This situation is exacerbated when chemical modification of the free tail groups leads to stronger adhesion forces at the interface and hence much greater force gradients [9, 10]. Finally, the finite mechanical coupling between the normal and lateral force sensing modes of a typical AFM cantilever [23] must also be taken into account in examining the friction-load relation of model lubricants.

In this section, we describe a new way of examining frictional forces over the *entire* adhesion interaction between a probe tip and the sample surface that not only avoids the inherent mechanical instabilities of AFM cantilevers, but also completely decouples normal and lateral force sensors. The method is based on bringing together the techniques of shear-force microscopy [24, 25] with the IFM. In this arrangement, frictional forces acting to dampen the tip's lateral motion are monitored independently as a function of both positive (repulsive) and negative (attractive) loads. Thus the adhesion nature of friction at the earliest stages of contact can be clearly characterized. Experimental details have been published elsewhere [26], but the basic design is to mount the probe tip shown in Fig. 3 on a small "dither" piezo tube, which vibrates it laterally. The probe is made of a glass fiber which provides a fairly high figure of merit $Q = m\omega/R \approx 100$, where ω is the natural resonance frequency (25–50 kHz), m is the fiber mass, and R is the damping out of contact. The diameter of the probe tip is reduced to <100 nm by using a commercial fiber puller [27]. Fiber motion induces voltages on the piezo tube, which are detected on the remaining quadrants by a phase-sensitive lock-in amplifier [28]. Attenuation of the fiber amplitude upon interaction of the probe tip with the surface is the basis for our friction measurements. The shear force damping (friction force) is proportional to the quantity $(1-V/V_0)$, where V is the attenuated signal at a given displacement and V_0 is the unattenuated signal due to the free lateral amplitude prior to contact [26]. For an initial 12 nm free amplitude, we estimate that the frictional force at complete damping is 18 nN [26]. By keeping the initial free amplitude constant, we in effect use the *same range of friction force* (0–18 nN) for each sample. (For much higher normal loads and lateral forces, another technique has been recently developed involving lateral force detection by the IFM itself [29].)

We have studied the behavior of two thiols discussed above which have identical chain lengths, but differing tail groups: $CH_3(CH_2)_{11}SH$ (hereafter called "CH_3-thiol"), and $COOH(CH_2)_{11}SH$ (hereafter called "COOH-thiol"). Although the chemistry of the bare glass tip can be modified in principle, we choose here to let the native glass silanol groups interact with the molecular monolayers; therefore, our functional group "pairings" are CH_3 *vs.* OH and COOH *vs.* OH. All of the experiments were conducted in a filtered, dry nitrogen atmosphere where the relative humidity was less than 8%, and no capillary condensation of water was observed.

We show at the top of Fig. 5 the lateral "shear" damping of the tip amplitude as the oscillating fiber approaches the CH_3-thiol monolayer, together with the *simultaneous* normal-force response of the IFM sensor. The tip approaches the substrate at a rate of 0.25 nm/s until the extent of lateral damping exceeds 80% of the undamped amplitude, at which point the tip is withdrawn at the same rate. We estimate the displacement is accurate to within 15%, with independent piezo tube calibration performed against a known 5 nm feature. Unlike Fig. 4, we now arbitrarily set zero in the displacement axis in Fig. 5 to be the point where the damping (friction) begins. (Also, the direction of approach is now right to left, instead of left to right). The initially negative IFM sensor signal indicates a weak attractive interaction that reaches a maximum of ~100 nN, and appears to have a total range of 0.7±0.1 nm. As the tip continues to approach past approximately (-0.7 nm), the attractive interaction gives way to increasingly repulsive forces that compress the CH_3-thiol monolayer and gold

substrate. A JKR force-displacement fit in this ~3.2 nm compressive regime provides an effective Young"s modulus of 8±1 GPa that is comparable to a value of 9.3±3.1 GPa previously measured for a supported hydrocarbon film [30]. Thus, in summary, friction in the CH_3-thiol system is due first to weak attractive forces, followed by compression of the film.

Under identical conditions and approach rate, the interaction of the *same tip* with the COOH-thiol sample is predominantly attractive; as shown in the lower part of Fig. 5, the tip motion is completely damped over the same range of lateral forces long before any appreciable repulsive compression occurs. In fact, the steep rise in friction with displacement suggests that a significant fraction of COOH-thiol chains "stand up" from their usual 30° tilt [12] to meet the probe. The ~0.7 nm range of the tip-COOH-thiol attractive interaction is essentially the same as that observed for the CH_3-thiol, although the forces are clearly much stronger. Thus it is possible that some of the CH_3-thiol chains stand up as well, but they are unable to significantly slow the tip down because of the relatively weak attractive interaction. However, by virtue of the stronger attractive interaction, the COOH-thiols bring the tip to a halt. The collective motion of the chains will act as an efficient channel for vibrational energy dissipation in addition to the losses incurred by the making and breaking of adhesion bonds. We can account for ~0.3 nm of the ~0.7 nm attractive interaction range through the motion of the thiol chains from the initial 30° tilt to a 0° upright position. The additional ~0.4 nm could be due to surface roughness over the ±12 nm lateral motion.

If we examine the data in terms of shear damping (friction) *vs.* load (Fig. 6), the adhesion difference between the two thiols is readily apparent. The JKR model predicts the dependence of tip-sample contact area A upon the applied load L. Thus, assuming friction F is proportional to contact area through a constant shear strength τ, we have the relation given in Equation 5 for a parabolic tip,

$$F = \tau A = \tau\pi\left\{\frac{R}{K}\left[L + 3\pi R W_A + \sqrt{6\pi R W_A L + (3\pi R W_A)^2}\right]\right\}^{2/3} \tag{5}$$

where

$$K = \frac{4}{3}\left(\frac{1-\nu_1^2}{E_1} + \frac{1-\nu_2^2}{E_2}\right)^{-1}. \tag{6}$$

The reduced modulus K of the two materials in contact (Equation 6) is a function of the respective Young's moduli (E_1, E_2) and Poisson ratios (ν_1, ν_2) of the tip and sample. If R and K are known, a plot of friction *vs.* load can be used to determine both constants W_A and τ. Since our glass tips were determined beforehand by scanning electron microscopy to be blunt and non-parabolic, we must apply the extensions to Equation (5) developed in Ref. [31]. As mentioned above, the JKR model also predicts the relationship between load and displacement, which yielded a value of E_1=8 GPa. If we assume ν_1=0.4 as for most materials, and use the (E_2, ν_2 of glass [32], weobtain K=11 GPa. With this value of K in the extensions to Equation (5), we observe the JKR friction *vs.* load fits shown in Fig. 6 for CH_3-thiol and COOH-thiol. Although adhesion hysteresis was observable, approach and withdrawal JKR fits were the same within experimental error.

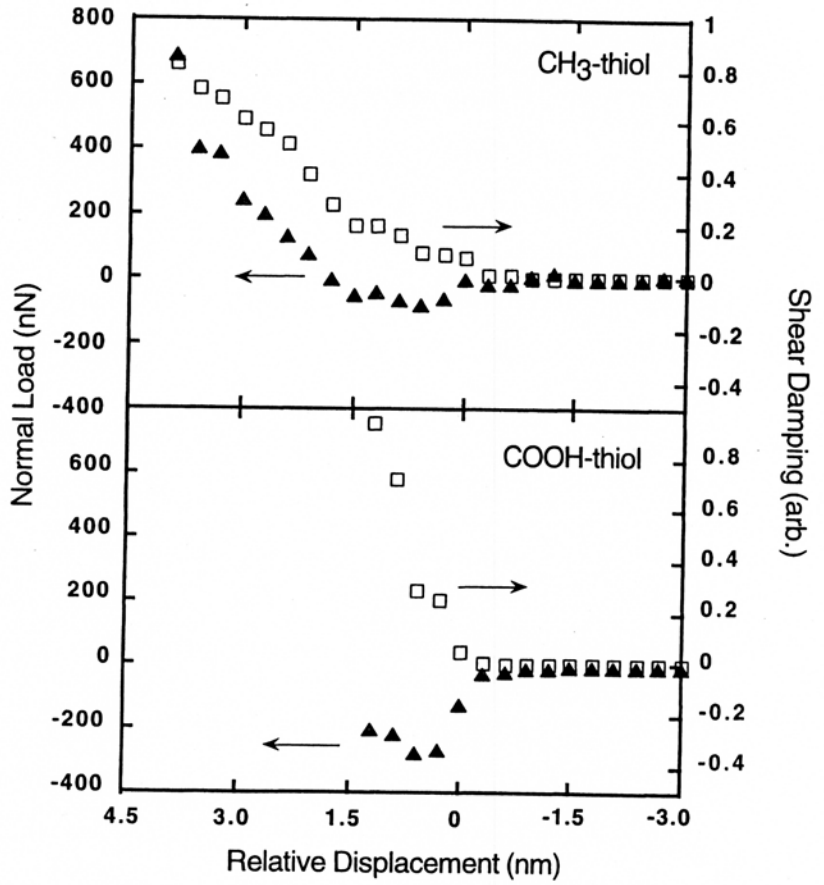

Figure 5. Simultaneous shear damping of tip lateral motion (□) and normal forces (▲) on tip acquired for approach to CH_3-thiol monolayer (top) and to COOH-thiol monolayer (bottom). The same glass tip, terminated by intrinsic silanols, is used for both data sets. The corresponding withdrawal curves are not shown for the sake of clarity. Zero displacement is arbitrarily set at the point of initial contact, and the approach is from right to left.

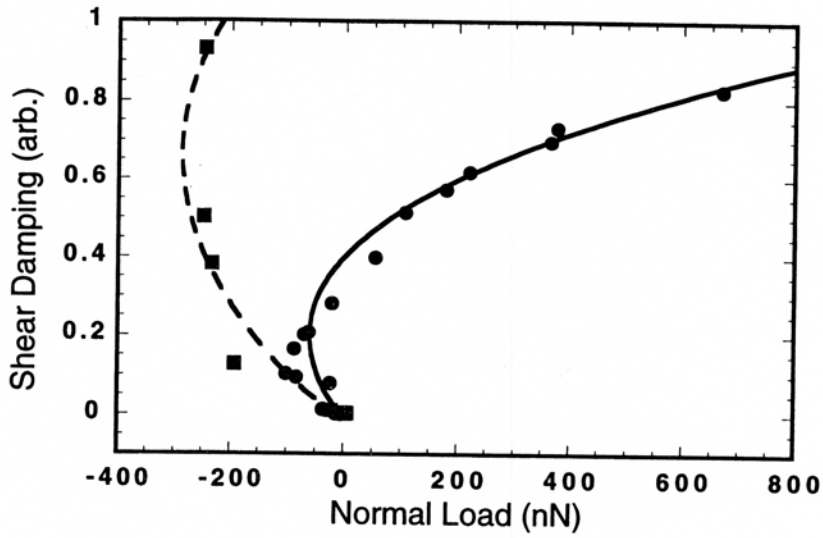

Figure 6. Johnson-Kendall-Roberts (JKR) fits to shear damping (friction) *vs.* normal load for different monolayers: (●-solid curve) CH_3-thiol, and (■-dashed curve) COOH-thiol.

Averaging over many fits for different regions of the CH_3-thiol monolayer, we obtain $W_A = 50\pm21$ mJ/m^2, which is in better agreement with purely van der Waals molecular interactions [17] than observed in the previous section. The COOH-thiol monolayer has an average adhesion energy $W_A = 449\pm49$ mJ/m^2 with the glass silanol groups, which we see from Table 1 is stronger than the COOH *vs.* COOH pair, but weaker than the COOH vs. NH_2 pair. If we subtract the 50 mJ/m^2 van der Waals contribution, the 400 mJ/m^2 result yields a hydrogen-bond energy of ~12 kcal/mole.

From $F = 18$ nN at 100% damping and the contact areas given by the fits [33], we obtain average shear strength (τ) values of 13.7±1.4 MPa and 20.0±1.9 MPa for CH_3-thiol and COOH-thiol, respectively. The CH_3-thiol shear strength is similar to those obtained for hydrocarbon films with the surface forces apparatus [34]. It is initially surprising that the difference in shear strengths for the CH_3-thiol and COOH-thiol does not correspond with the large difference in adhesion. However, the JKR fit for the CH_3-thiol includes a significant portion of positive applied loads, whereas the JKR fit for COOH-thiol only has negative loads. The absence of data in the repulsive contact regime for the COOH-thiol could mean that the JKR fit provides a lower bound to the estimated shear stress. More important is the fact that the JKR model assumes that the interfacial forces have zero spatial range. Models other than DMT which allow a small, finite range to these attractive forces [35] produce curves essentially the same as those depicted in Fig. 6, and predict that contact is first made with the surface displaced significantly upward from its equilibrium position, i.e. there is tensile deformation of the surface toward the tip. Indeed, observing finite friction with such negative loads indicates that the materials have made contact under tensile stress and thus the "range" of attractive forces should take account of film deformation as the molecules extend upward in response to the attractive forces. Our observations are unique, since measurements of load, displacement and friction in this tensile, molecularly-deformed regime are not possible with sensors exhibiting jump-to-contact instabilities.

4. SUMMARY AND CONCLUSIONS

Scanning force microscopy is ideally suited for fundamental studies of acid–base interactions at the molecular-level. In particular, we have focused on the interfacial force microscope (IFM), which avoids mechanical instabilities such as "jump-to-contact" that affect cantilever-based atomic force microscopes (AFM). With the non-compliant IFM, one is able to map the entire adhesion interaction *vs.* displacement and also reveal the extent of adhesion hysteresis. Furthermore, we have discussed the sensitivity of IFM to measure the magnitude of adhesion forces between functionalized self-assembled monolayers which range from weak van der Waals dispersion forces to "full strength" acid–base (hydrogen-bonding).

We have shown that the molecular origins of friction can be examined in detail with an instrument which combines the IFM with shear-force microscopy in a way that decouples normal and lateral force sensors. Correlation of normal forces with lateral shear forces reveals both the attractive and repulsive nature of friction between the contacting surfaces. Chemical modification of the surface dramatically changes the relative contributions of adhesion forces to friction. In addition to dissipative processes due to bond

breaking and making, strong adhesion forces may result in additional channels of energy loss characterized by tensile deformation and collective chain motion. Studies such as those presented here can help reveal the detailed relationship between friction and adhesion, and identify modes of deformation unique to molecular films.

Acknowledgments

R. W. C. acknowledges support from the Natural Sciences and Engineering Research Council of Canada. Sandia is a multiprogram laboratory operated by Sandia Corporation, a Lockheed Martin Company, for the United States Department of Energy under Contract DE-AC04-94AL85000.

REFERENCES

1. G. S. Blackman, C. M. Mate, and M. R. Philpott, *Phys. Rev. Lett.* **65**, 2270 (1990).
2. N. A. Burnham, D. D. Dominguez, R. L. Mowery, and R. J. Colton, *Phys. Rev. Lett.* **64**, 1931 (1990).
3. N. A. Burnham, R. J. Colton, and H. M. Pollock, *Nanotechnology* **4**, 64 (1993).
4. S. A. Joyce and J. E. Houston, *Rev. Sci. Instrum.* **62**, 710 (1991).
5. R. C. Thomas, J. E. Houston, R. M. Crooks, T. Kim, and T. A. Michalske, *J. Amer. Chem. Soc.* **117**, 3830 (1995).
6. J. Krim, *Sci. Amer.* **275**, 74 (1996).
7. R. W. Carpick and M. Salmeron, Chem. Rev. **97**, 1163 (1997).
8. G. Hähner and N. Spencer, *Phys. Today* **51**, 22 (Sept. 1998).
9. C. D. Frisbie, L. F. Rozsnyai, A. Noy, M. S. Wrighton, and C. M. Lieber, *Science* **265**, 2071 (1994).
10. A. Noy, D. V. Vezenov, and C. M. Lieber, *Annu. Rev. Mater. Sci.* **27**, 381 (1997).
11. J.-B. D. Green, M. T. McDermott, M. D. Porter, and L. M. Siperko, *J. Phys. Chem.* **99**, 10960 (1995).
12. L. H. Dubois and R. G. Nuzzo, Annu. *Rev. Phys. Chem.* **43**, 437 (1992).
13. A. Ulman, *Chem. Rev.* **96**, 1533 (1996).
14. A. Lio, D. H. Charych, and M. Salmeron, *J. Phys. Chem. B* **101**, 3800 (1997).
15. N. D. Shinn, T. Kim, C. Daly, T. Mayer, R. Crooks, and T. Michalske, *Langmuir*, in press.
16. R. G. Horn, J. N. Israelachvili, and F. Pribac, *J. Colloid Interface Sci.* **115**, 480 (1986).
17. J. N. Israelachvili, *Intermolecular and Surface Forces.* Academic Press, London (1992).
18. O. L. Warren, J. F. Graham, and P. R. Norton, *Rev. Sci. Instrum.* **68**, 4124 (1997).
19. K. L. Johnson, K. Kendall, and A. D. Roberts, *Proc. Roy. Soc. Lond. A* **324**, 301 (1971).
20. B. V. Derjaguin, V. M. Muller, and Yu. P. Toporov, *J. Colloid Interface Sci.* 53, 314 (1975).
21. F. M. Fowkes, *J. Phys. Chem.* **66**, 382 (1962).
22. G. C. Pimentel and A. L. McClellan, *The Hydrogen Bond.* W. H. Freeman and Co., San Francisco (1960).
23. D. F. Ogletree, R. W. Carpick, and M. Salmeron, *Rev. Sci. Instrum.* **67**, 3298–3306 (1996).
24. E. Betzig, P. L. Finn, and J. S. Weiner, *Appl. Phys. Lett.* **60**, 2484 (1992).
25. R. Toledo-Crow, P. C. Yang, Y. Chen, and M. Vaez-Iravani, *Appl. Phys. Lett.* **60**, 2957 (1992).
26. A. R. Burns, J. E. Houston, R. W. Carpick, and T. A. Michalske, *Langmuir* **15**, 2922 (1999).
27. Sutter Instruments, Novato, CA.
28. J. Barentz, O. Hollricher, and O. Marti, *Rev. Sci. Instrum.* **67**, 1912 (1996).
29. J. D. Kiely and J. H. Houston, *Langmuir* **15**, 4513 (1999).
30. T. P. Weihs, Z. Nawaz, S. P. Jarvis, and J. B. Pethica, *Appl. Phys. Lett.* **59**, 3536 (1991).
31. R. W. Carpick, N. Agraït, D. F. Ogletree, and M. Salmeron, *J. Vac. Sci. Technol. B* **14**, 1289 (1996).
32. H. Muramatsu, N. Chiba, and M. Fujihira, *Appl. Phys. Lett.* **71**, 2061 (1997).
33. ~400 nm^2 at the minimum load. This area is smaller than the tip shape, due to small asperities and/or surface roughness.
34. J. N. Israelachvili, in: *Handbook of Micro/Nanotribology,* B. Bhushan (Ed.), p. 267. CRC Press, Boca Raton, FL (1995).
35. J. A. Greenwood, *Proc. R. Soc. Lond. A* **453**, 1277 (1997).